Simulation of Lueders bands using regularized large strain elasto-plasticity

M. MUCHA, B. WCISŁO, J. PAMIN

Chair for Computational Engineering, Cracow University of Technology,
Warszawska 24, 31-155 Cracow, email: mmucha@cce.pk.edu.pl

THIS PAPER DEALS WITH THE NUMERICAL SIMULATION of an instability phenomenon called Lueders bands with two regularized material models: viscoplasticity and gradient-enhanced plasticity. The models are based on large strain kinematics and temperature-dependence is incorporated. The Huber–Mises–Hencky yield condition and multi-branch hardening are employed. After a brief presentation of the constitutive description, test computations are performed using AceGen and AceFEM symbolic packages for Wolfram Mathematica. The first benchmark is a rectangular tensile plate in plane strain isothermal conditions. For the viscoplastic model, simulation results for different values of viscosity, loading duration and enforced displacement are compared. For the gradient model different internal lengths are used. Mesh sensitivity of the results and the influence of boundary conditions are also examined. Next to the Lueders-type response to a softening-hardening yield strength function, an additional softening stage leading to failure is also considered. The second example concerns a bone-shape sample under tension, for which, next to mesh sensitivity and the effect of regularization, the influence of heat conduction on simulation results is evaluated.

Key words: Lueders bands, viscoplasticity, gradient plasticity, thermo-mechanical coupling, parametric study.

1. Introduction

IN THIS PAPER TWO DIFFERENT LARGE STRAIN MODELS, viscoplasticity and gradient-enhanced plasticity are used to simulate a propagative instability phenomenon called Lueders bands. Lueders bands occur in metallic materials, e.g. in low-carbon steel, around room temperature. The phenomenon is described in several publications, see for instance [1–3] and references therein. Although Lueders-like instabilities usually have a transient character, their understanding is important, since as other instability phenomena they are related to degradation of the material properties and/or structural performance.

In many metals and alloys a softening stage (yield a stress drop) follows the initiation of the plastic process. The observed process continues with a plastic flow plateau and then hardening occurs. Considering the current tangent

stiffness, it is negative, zero and positive in the three stages, respectively. As explained by Cottrell [1], this plastic process is related to stress wave propagation, the front part of the plastic wave slows down while the later part still travels to form a sharp plastic front, called the Lueders front. It can be viewed as a strain discontinuity, although it rather has a non-zero width.

The phenomenon is treated here as initiated by material softening although geometrical softening due to large deformations is included in the analysis. Simulation of instabilities and localized deformation can involve pathological discretization sensitivity, hence a regularization of the constitutive description is necessary. Strain rate sensitivity is known to increase ductility and stabilize the response of plastic materials, hence viscoplasticity is the main constitutive framework employed in [4–6]. An alternative regularization is provided by a gradient-type enhancement [7, 8].

However, thermal softening which occurs in majority of elasto-plastic materials with a temperature increase can also trigger an unstable behaviour, and heat conduction can influence evolving strain localization [9, 10]. Therefore, the models employed in this study are formulated as temperature-dependent. It is mentioned in this context that high strain rates can induce a different instability phenomenon, not considered here: multiple localization zones called adiabatic shear bands, cf. [11–13].

The reader interested in the microstructural origins of Lueders bands (related to travelling atoms and dislocations) are referred to [2] and references to the works of Cottrell et al. as well as Hall et al. given there. The Lueders-type phenomena were analyzed experimentally using low-carbon steel in [14–16]. Both experiments and numerical modelling were performed in [17–19]. In [17] a viscoplastic model was employed, in [19] a gradient plasticity model was applied. Moreover, in [20] Lueders bands have been simulated in shape memory alloys using a micromorphic gradient-enhanced model.

To set the stage broader, we recall the classification of instability types proposed in [2] and discussed in [21–23] assuming linear kinematics. For simplicity we also limit here this brief presentation to a rate-dependent isothermal plasticity model (gradient term is additionally included in [21–23]). Consider the equation of wave propagation in a bar (dot over a symbol denotes time derivative):

$$(1.1) \qquad \frac{\partial \dot{\sigma}}{\partial x} = \rho \frac{\partial^2 v}{\partial t^2}, \qquad v = \dot{u}, \qquad \dot{\epsilon} = \frac{\partial v}{\partial x}.$$

Here σ is the stress, ρ is the density, u denotes the displacement and thus v is the velocity. For elastic-plastic flow we have the following decomposition:

$$(1.2) \qquad \dot{\epsilon} = \dot{\epsilon}^e + \dot{\epsilon}^p, \qquad \dot{\sigma} = E\dot{\epsilon}^e$$

where E is Young's modulus. The analysis is expanded to viscoplasticity:

$$(1.3) \qquad \sigma = \sigma(\epsilon^p, \dot{\epsilon}^p), \quad \dot{\sigma} = H\dot{\epsilon}^p + S\ddot{\epsilon}^p, \quad H = \frac{\partial \sigma}{\partial \epsilon^p}, \quad S = \frac{\partial \sigma}{\partial \dot{\epsilon}^p}$$

denoting the hardening modulus by H and the strain-rate dependence factor by S. When the above equations are substituted into Eq. (1.1) one obtains the equation of dynamics as follows:

$$(1.4) \qquad H\hat{\nabla}\dot{\epsilon}^p + S\hat{\nabla}\ddot{\epsilon}^p = \rho\frac{\partial^2 \dot{\epsilon}^p}{\partial t^2}, \quad \hat{\nabla} = \frac{\partial^2}{\partial x^2} - \frac{\rho}{E}\frac{\partial^2}{\partial t^2}.$$

The stability of deformation can be examined by perturbing the uniform strain with

$$(1.5) \qquad \delta\dot{\epsilon}^p = \delta\epsilon_0 e^{ikx+\omega t}$$

where k is the wave number and ω is the eigenvalue. Upon substitution of the perturbation into Eq. (1.4) one obtains the equation:

$$(1.6) \qquad \omega^3 + a\omega^2 + b\omega + c = 0, \quad a = \frac{E+H}{S}, \quad b = \frac{E}{\rho}k^2, \quad c = \frac{E}{\rho}k^2\frac{H}{S}.$$

When one of the Routh–Hurwitz conditions $a > 0$, $c > 0$, $ab - c > 0$ is not satisfied, the function $\omega(k)$ has a positive real part, the perturbation grows and the deformation is unstable. One can then distinguish:

1. Instability of type H for $H < 0$, $S > 0$ (stationary, called in [22] static). This involves softening in relation $\sigma(\epsilon)$ (strain softening), which triggers stationary localization bands. In fact, such bands can also be induced by a non-symmetric material tangent operator, as commonly happens in geomaterials, cf. [24].

2. Instability of type S for $H > 0$, $S < 0$ (called in [22] propagative). This involves softening in relation $\sigma(\dot{\epsilon})$ (strain rate softening) and produces a discontinuous plastic process which can have the form of Portevin–Le Chatelier bands (PLC effect).

However, considering the yield strength function and referring to a typical plastic response of metal specimens in tension, sketched in Fig. 1, after passing an upper yield limit σ_U the softening response occurs down to a lower yield limit σ_L, while a stationary shear band is formed. The softening stage is followed by an ideal plasticity stage and hardening ($H \geq 0$). The shear band then travels through the specimen, so the Lueders-type response has a propagative nature, although it is not a dynamic phenomenon. Therefore, the authors of this paper are of the opinion that the Lueders-type response forms an additional class of instabilities,

say type L (H evolves from softening to hardening while $S > 0$). It is mentioned that the authors of [2] distinguish additionally type T instabilities caused by thermal softening, but they can be classified in the broad group of type H instabilities.

As noted in [3], the process is described by so-called Lueders parameters σ_U, σ_L and ϵ_L (so-called Lueders strain) which depend on material composition and microstructure, temperature and strain rate. The last two aspects are considered in this study.

It was noticed for instance in [19, 25] that the simulation of type L of localization phenomenon requires regularized continuum models, therefore we employ two such models in this paper: the first one contains viscous terms and the second one is enhanced by spatial gradients. The two enhancements should guarantee not only mesh-insensitive simulation results, but also a finite (non-zero) width of propagating Lueders bands. To check the influence of temperature on the process, the models are formulated in a temperature-dependent format. As known already from [9, 10] and shown recently in [26], heat conduction can also provide regularization, unless an adiabatic limit of a thermo-mechanical process is approached.

The aim of this paper is phenomenological modelling and the assessment of the potential of the selected large strain constitutive models [27, 28] in the simulation of the qualitative features of the Lueders phenomenon. Therefore, no model validation is attempted, although it is undoubtedly an important task for the future. We do not discuss the issues of band direction or velocity either. The phenomenon is analyzed as plastic front propagation, simulated assuming quasi-static conditions, i.e. neglecting inertia effects. However, we additionally analyze the final softening stage after hardening which leads to necking and the specimen failure.

The viscoplastic model is based on the consistency approach, see [21], however it accounts here for large strains. The gradient enhanced model is based on [8]. The models are implemented using the AceGen symbolic package for Wolfram Mathematica [29, 30]. The analyses are performed using standard Newton algorithms with automatic load stepping within the AceFEM finite element solver. Three-dimensional models are employed.

The paper is organized as follows. Section 2 contains a short presentation of the employed models and multi-branch hardening laws. In Section 3 the simulation results are presented for the benchmark test of a plate satisfying plane strain conditions, subjected to uniaxial tension (a three-dimensional model is used to represent a two-dimensional test). The isothermal process is assumed and the following aspects are investigated: ability of the regularized constitutive models to simulate Lueders bands, influence of mesh density, viscosity (strain rate), internal length and boundary conditions on the results. Some viscoplastic model simulations are repeated for the whole plate to investigate whether imposed symmetry

affects the results. The case with final softening is included to present a simple model which enables the simulation of sample failure. In Section 4 the computation results are presented for a bone-shape plate sample under tension (a three-dimensional model is used, i.e. plane stress conditions are assumed). The computations are first performed for the viscoplastic and gradient-enhanced model in isothermal conditions, and then for the general thermo-viscoplastic model and the gradient enhanced thermo-plasticity. Section 5 contains the conclusions.

The following novelties in the paper can be pointed out:

- Large strain viscoplasticity and gradient-enhanced plasticity models are implemented in Ace for Mathematica to simulate the phenomenon of Lueders bands in metallic materials. The regularized models are formulated as temperature-dependent, which enables the analysis of the influence of heat conduction on the process.
- In a parametric study the influence of several factors on the simulated localized deformation history is analyzed. This leads to conclusions concerning the regularization efficiency and selected modelling issues.
- The second benchmark with the geometry designed to enable future experimental analysis examines the response of the models for isothermal, conductive and adiabatic conditions.

2. Brief description of constitutive models

2.1. Thermo-plasticity

Figure 1 shows an idealized relation of the nominal stress and the averaged strain for a specimen exhibiting Lueders band propagation. At the beginning of a localized plastic process, when softening starts, a stationary band arises at the upper yield limit σ_U. At the lower yield stress σ_L a plastic front forms and the band starts to propagate through the sample. As it passes, the plastic strains accumulate along the sample and reach the so-called Lueders strain ϵ_L. At the end of the process the deformation can become almost uniform due to hardening.

The material models used in the simulation of such a response are summarized below, they are based on large strain formulations [8, 31, 32].

A deformable continuous, isotropic body is considered, for which the vector $\mathbf{X}$ identifies the referential location of a body particle at time t_0 and temperature T_0, while vector $\mathbf{x}$ denotes the current position of the particle $\mathbf{X}$ at time t and temperature T. The function $\mathbf{x} = \boldsymbol{\varphi}(\mathbf{X}, t, T)$ describes the motion of the body. The deformation gradient $\mathbf{F}$ is defined as

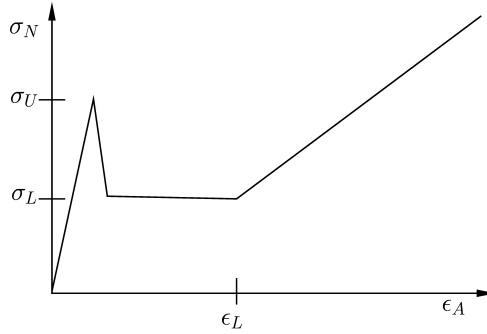$$(2.1) \qquad \mathbf{F} = \frac{\partial \boldsymbol{\varphi}(\mathbf{X}, t, T)}{\partial \mathbf{X}}.$$

Fig. 1. Simplified nominal stress vs. averaged strain relation for specimen deformation involving Lueders effect.

A decomposition of the deformation gradient into the elastic part $\mathbf{F}^e$, the plastic part $\mathbf{F}^p$ and the thermal part $\mathbf{F}^\theta$ is performed (see [33–35])

$$(2.2) \qquad \mathbf{F} = \mathbf{F}^e \mathbf{F}^p \mathbf{F}^\theta = \mathbf{F}^m \mathbf{F}^\theta,$$

where $\mathbf{F}^m$ is the mechanical part of the deformation gradient [32, 36]. The thermal contribution $\mathbf{F}^\theta$ is assumed to be purely volumetric and is defined as

$$(2.3) \qquad \mathbf{F}^\theta = (J^\theta)^{1/3}\mathbf{I}, \quad J^\theta = \det(\mathbf{F}^\theta),$$

where $\mathbf{I}$ is the second order identity tensor and the deformation caused by the temperature change is specified in the following form [35]

$$(2.4) \qquad J^\theta = e^{3\alpha_T(T-T_0)}.$$

In Eq. (2.4) α_T is the coefficient of linear thermal expansion.

Based on decomposition (2.2) and assumption (2.4) the mechanical part of the deformation gradient can be determined as

$$(2.5) \qquad \mathbf{F}^m = e^{-\alpha_T(T-T_0)}\mathbf{F}.$$

The illustration of the deformation decomposition can be found in [26].

For the classical rate and gradient-independent theory the Helmholtz potential per unit volume in reference configuration is decomposed additively into elastic, plastic and purely thermal parts (see [31, 32])

$$(2.6) \qquad \psi(\mathbf{b}^e, \gamma, T) = \psi^e(\mathbf{b}^e) + \psi^p(\gamma) + \psi^\theta(T).$$

The following forms of the potential components are adopted

$$(2.7) \qquad \psi^e(\mathbf{b}^e) = \frac{1}{2}G\big(\mathrm{tr}(\det(\mathbf{b}^e)^{-1/3}\mathbf{b}^e) - 3\big) + \frac{1}{2}K(\ln(J^e))^2,$$

$$(2.8) \qquad \psi^p(\gamma) = \frac{1}{2}H\gamma^2,$$

$$(2.9) \qquad \psi^\theta(T) = c\bigg((T - T_0) - T \cdot \ln\bigg(\frac{T}{T_0}\bigg)\bigg),$$

where G and K are elastic moduli, $\mathbf{b}^e = \mathbf{F}^e(\mathbf{F}^e)^{\mathrm{T}}$ is the elastic left Cauchy–Green tensor, $J^e = \det(\mathbf{F}^e)$.

The second component of the free energy is for simplicity expressed as a quadratic function of a scalar equivalent plastic strain γ, but in general it depends on adopted hardening specification. Moreover, c is the heat capacity.

The Kirchhoff stress tensor and hardening function are derived from the free energy potential

$$(2.10) \qquad \boldsymbol{\tau} = 2\frac{\partial\psi}{\partial\mathbf{b}^e}\mathbf{b}^e, \quad h = \frac{\partial\psi}{\partial\gamma}.$$

According to [37] the heat capacity can be defined as $c = -T\frac{\partial^2\psi}{\partial T^2}$ and therefore for the adopted form of free energy the capacity c is constant.

The constitutive relation for heat conduction is the classical Fourier law for isotropic materials, which is formulated here using the Kirchhoff heat flux vector $\mathbf{q}$

$$(2.11) \qquad \mathbf{q} = -k\nabla T,$$

where k is a heat conduction coefficient specified in the reference configuration and ∇T is a spatial gradient of temperature.

In this paper the yield function is defined as

$$(2.12) \qquad F_p(\boldsymbol{\tau}, \gamma, \dot{\gamma}, \omega) = f(\boldsymbol{\tau}) - \sigma_y(\gamma, \dot{\gamma}, \omega) \leq 0,$$

where $f(\boldsymbol{\tau})$ is the Huber–Mises–Hencky (HMH) stress measure and σ_y is assumed to represent multi-branch hardening described separately for the viscoplastic model (dependent on the plastic strain rate $\dot{\gamma}$) and the gradient-enhanced model (where damage-like variable ω reduces the yield strength) in the subsections below. It is noted that a model that would combine the two regularization effects is not considered in this paper, although this possibility was discussed for instance in [22, 38]. The following definitions are used

$$(2.13) \qquad f(\boldsymbol{\tau}) = \sqrt{2J_2},$$

$$(2.14) \qquad J_2 = \frac{1}{2}\boldsymbol{\tau}_{dev}^2 \cdot \mathbf{I},$$

where $\boldsymbol{\tau}_{dev}$ is a deviatoric part of the Kirchhoff stress tensor.

Following [31], the associated flow rule is adopted for the Lie derivative of $\mathbf{b}^e$

$$(2.15) \qquad \frac{1}{2}\mathcal{L}_v\mathbf{b}^e = \dot{\lambda}\mathbf{N}\mathbf{b}^e,$$

where $\mathbf{N}$ is the normal to the yield surface in the material configuration and $\dot{\lambda}$ denotes the plastic multiplier satisfying the standard Kuhn-Tucker conditions:

$$(2.16) \qquad \dot{\lambda} \geq 0, \quad F_p \leq 0, \quad \dot{\lambda}F_p = 0.$$

The conditions are also satisfied for the regularized models. The plastic multiplier plays the role of the plastic strain measure $\dot{\gamma} = \dot{\lambda}$. It is emphasized that due to large deformations geometrical softening is present in the description, see [39].

Due to the distinction between the reference and the current configurations in large strain analysis the governing equations can be formulated in the material description, see e.g. [40], or in the spatial description, e.g. [37]. In the present model the spatial quantities are used. However, they are referred to the volume/surface in the reference configuration, see e.g. [41].

The two governing equations which describe the analyzed coupled problem are the balance of linear momentum written in the local form in Eq. (2.17) and the energy balance presented in the temperature form in Eq. (2.18)

$$(2.17) \qquad \rho_0 \frac{\partial^2 \boldsymbol{\varphi}}{\partial t^2} = J \operatorname{div}(\boldsymbol{\tau}/J) + \rho_0\mathbf{y},$$

$$(2.18) \qquad c\frac{\partial T}{\partial t} = J \operatorname{div}(-\mathbf{q}/J) + \mathcal{R}.$$

In Eq. (2.17) $\operatorname{div}(\cdot)$ is the divergence computed with respect to Eulerian coordinates, ρ_0 is the reference density and $\mathbf{y}$ is a given spatial body force field. For the static analysis which is presented in the paper the left–hand side of Eq. (2.17) is equal to zero.

In Eq. (2.18) $\mathcal{R}$ is a heat source density. In the adopted model it includes heating due to plastic dissipation and has the following form [32]

$$(2.19) \qquad \mathcal{R} = \sqrt{\frac{2}{3}}\chi\sigma_y\dot{\gamma}.$$

The parameter χ in Eq. (2.19) denotes a dissipation heat factor which for simplicity is assumed to be constant, cf. [42]. The balance of linear momentum (2.17) is completed with boundary conditions for displacements $\mathbf{u}$ and tractions $\mathbf{t}$:

$$(2.20) \qquad \begin{aligned} \mathbf{u} &= \hat{\mathbf{u}} && \text{on } \partial\mathcal{B}_u, \\ \mathbf{t} = \boldsymbol{\tau}\cdot\mathbf{n} &= \hat{\mathbf{t}} && \text{on } \varphi(\partial\mathcal{B}_\tau), \end{aligned}$$

where $\mathbf{n}$ is the normal to the body surface and as usual

(2.21) $$\partial\mathcal{B}_u \cup \partial\mathcal{B}_\tau = \partial\mathcal{B} \quad \text{and} \quad \partial\mathcal{B}_u \cap \partial\mathcal{B}_\tau = \emptyset.$$

The energy balance equation (2.18) is also complemented with appropriate boundary conditions:

(2.22)
$$T = \hat{T} \quad \text{on } \partial\mathcal{B}_T,$$
$$\mathbf{q} \cdot \mathbf{n} = \hat{q} \quad \text{on } \boldsymbol{\varphi}(\partial\mathcal{B}_q),$$

where

(2.23) $$\partial\mathcal{B}_T \cup \partial\mathcal{B}_q = \partial\mathcal{B} \quad \text{and} \quad \partial\mathcal{B}_T \cap \partial\mathcal{B}_q = \emptyset.$$

The weak forms of the governing equations are the basis for the finite element implementation. Applying the standard derivation: multiplication by the test function $\delta\mathbf{u}$, integration over the volume of body $\mathcal{B}$, application of divergence theorem and Neumann boundary conditions, the balance of linear momentum has the following weak form

(2.24) $$\int_\mathcal{B} (\nabla\delta\mathbf{u} : \boldsymbol{\tau} + \delta\mathbf{u} \cdot \mathbf{B})\,\mathrm{d}V + \int_{\boldsymbol{\varphi}(\partial\mathcal{B}_\tau)} \delta\mathbf{u} \cdot \hat{\boldsymbol{t}}\,\mathrm{d}a = 0.$$

The weak form of the energy balance equation (2.18) is also obtained using the standard procedure and the backward Euler scheme for time integration. The following integral equation is valid for the current time moment

(2.25) $$\int_\mathcal{B} \left(\delta T \frac{c}{\Delta t}(T - T_n) + \nabla\delta T k \nabla T - \delta T \mathcal{R}\right)\mathrm{d}V + \int_{\boldsymbol{\varphi}(\partial\mathcal{B}_q)} \delta T \hat{q}\,\mathrm{d}a = 0,$$

where T_n is the value of temperature at the previous time instant and Δt is the time increment.

2.2. Viscoplastic model

The viscoplastic model follows the consistency concept, cf. [21]. The yield function is defined as

(2.26) $$F_p(\boldsymbol{\tau}, \gamma, \dot{\gamma}, T) = f(\boldsymbol{\tau}) - \sigma_y(\gamma, \dot{\gamma}, T) \leq 0$$

and the yield strength for the isothermal case contains the following hardening function

(2.27) $$\sigma_y(\gamma, \dot{\gamma}) = \sqrt{2/3}(\sigma_{y0} + h(\gamma)) + \xi\dot{\gamma},$$

where ξ is viscosity. Please note that viscosity ξ has been denoted S in the Introduction.

It is assumed that the viscous term affects the hardening during the whole process, although viscosity provides numerical regularization rather than is treated as a physical property.

The top two diagrams in Fig. 2 show simplified multilinear models of yield strength evolution with the increase of a plastic strain measure $\sigma_y(\gamma)$ which are first used in this paper. According to the first diagram in Fig. 2, which was used in [21] and which mimics the specimen response in Fig. 1 we have

$$(2.28) \qquad h(\gamma) = \begin{cases} H_1\gamma, & \gamma \leq \gamma_1, \\ H_1\gamma_1, & \gamma_1 < \gamma < \gamma_2, \\ H_1\gamma_1 + H_2(\gamma - \gamma_2), & \gamma \geq \gamma_2, \end{cases}$$

with $H_1 < 0$ and $H_2 > 0$. However, as noticed in [20], "typical mechanical response exhibiting a stress plateau is often incorrectly interpreted as the material response, while it is in fact the response of a specimen, which is related to nucleation and propagation of macroscopic transformation fronts" – here the authors mean the Lueders front. Therefore, we also consider the second softening-hardening diagram shown in Fig. 2 on the top right ($\gamma_2 = \gamma_1$).
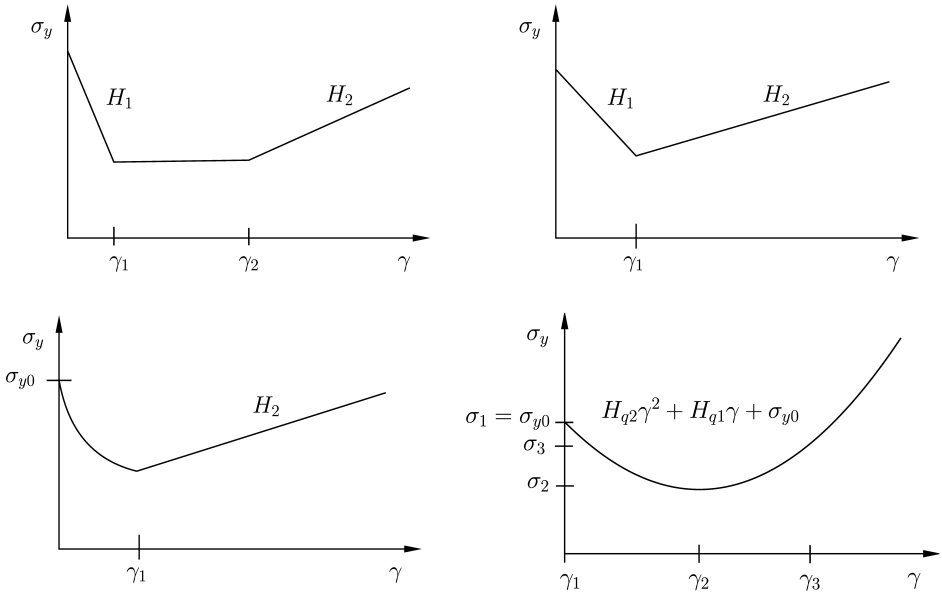
FIG. 2. Yield stress vs equivalent plastic strain relations: multi-linear used in viscoplastic model (top), and nonlinear used in isothermal gradient-enhanced model (bottom left), quadratic used in temperature-dependent case (bottom right).

For the thermo-viscoplastic model a smooth quadratic hardening function is adopted, see Fig. 2 bottom right. The yield strength is then defined as follows

$$(2.29) \qquad \sigma_y(\gamma, \dot{\gamma}, T) = \sqrt{2/3}[\sigma_{y0}(1 - H_T(T - T_0)) + H_{q2}\gamma^2 + H_{q1}\gamma] + \xi\dot{\gamma},$$

where H_{q2} and H_{q1} are quadratic hardening parameters calculated from three given points. The part $(1 - H_T(T - T_0))$ represents thermal softening in a simplified linear manner H_T is a thermal softening modulus. Different formulations of thermal softening and their numerical verification can be found in [43].

As has been mentioned, the introduction of viscosity can serve as a regularization method. As argued in [44], there is a material length associated with viscosity $l_v = \xi/\sqrt{E\rho}$, where ξ is viscosity [kg/(m · s)], E is the Young modulus [kg/(m · s^2)] and ρ is density [kg/m^3]. It is stated in [44] that "any rate dependence in the constitutive law combined with inertial effects introduces an internal length scale". However, "for load durations much larger than the relaxation (or retardation) time associated with the type of viscosity used, the modelling is not completely objective". This relaxation time is "the time of passage of a wave front over the distance l_v", so it is calculated as $\tau_0 = l_v/v = \xi/E$, where $v = \sqrt{E/\rho}$ is longitudinal elastic wave velocity. Thereby, it is remarked that since inertia forces are not incorporated in the analyses presented in this paper (ρ is not specified), we do not simulate wave propagation. Moreover, if viscosity is a known material parameter, and its value is too small to regularize the problem, the nonlocality is a proper option of model enhancement.

2.3. Gradient-enhanced plasticity model

The yield function for the gradient-enhanced thermo-plastic model is defined as an extension of the model of [8]

$$(2.30) \qquad F_p(\boldsymbol{\tau}, \gamma, \omega, T) = f(\boldsymbol{\tau}) - \sigma_y(\gamma, \omega, T) \leq 0,$$

where the yield strength for the isothermal case depends on a degradation parameter ω in the following way

$$(2.31) \quad \sigma_y(\gamma, \omega) = \begin{cases} \sqrt{2/3}(\sigma_{y0} + H_1\gamma)(1 - \omega), & \gamma \leq \gamma_1, \\ \sqrt{2/3}(\sigma_{y0} + H_1\gamma_1)(1 - \omega_1), & \gamma_1 < \gamma < \gamma_2, \\ \sqrt{2/3}(\sigma_{y0} + H_1\gamma_1 + H_2(\gamma - \gamma_2))(1 - \omega_1), & \gamma \geq \gamma_2, \end{cases}$$

while $H_1 \geq 0$ and $H_2 \geq H_1$ are now assumed since softening is induced by the plastic-degradation variable $\omega \in [0, 1]$. Its evolution is described by the following formula

$$(2.32) \qquad \omega = 1 - \exp(-\beta z),$$

where β is a ductility parameter and nonlocal variable z is obtained from the averaging equation [7]

$$(2.33) \qquad z - l^2 \nabla_0^2 z = \sqrt{2/3}\gamma$$

in which l is an internal length scale, ∇_0 is the gradient operator in material description. Thus, variable z has the interpretation of non-local (averaged) equivalent plastic strain, see [8], so Eq. (2.33) controls the localization of γ. It is mentioned that the yield strength degradation is frozen $\omega = \omega_1$ when $\gamma \geq \gamma_1$ to exclude further material softening. It is also emphasized that in the numerical solution algorithm the averaged plastic strain z is discretized in addition to displacements and two-field finite elements are used. Homogeneous natural boundary conditions are assumed as usual for Eq. (2.33).

For the gradient-enhanced thermo-plastic model the quadratic hardening similar to the thermo-viscoplastic model is used. The yield strength is defined as follows

$$(2.34) \qquad \sigma_y(\gamma, \omega, T) = \sqrt{2/3}[\sigma_{y0}(1 - H_T(T - T_0)) + H_{q2}\gamma^2 + H_{q1}\gamma](1 - \omega),$$

where H_{q2} and H_{q1} are square hardening parameters calculated from three given points. The part $(1 - H_T(T - T_0))$ is linear thermal softening, H_T is a thermal softening modulus. As in the isothermal case, the value of ω is frozen for $\gamma \geq \gamma_2$.

3. Numerical implementation

The whole process of the numerical implementation and testing is performed in Wolfram Mathematica packages called AceGen and AceFEM. The first package is used for the development of a user subroutine for the finite element method. The code is prepared in a special symbolic programming language, automatically translated and transferred to a chosen finite element environment (i.e. ABAQUS, FEAP), in this case to AceFEM. The main advantage of AceGen is its capability of automatic differentiation which is used for linearization of the governing equations. Usually, it is the most time consuming stage of code development. The detailed description of AceGen features and examples of usage can be found for example in [29]. In turn, AceFEM is chosen because of its perfect collaboration with AceGen and user-friendly pre- and postprocessing.

An extensive description of the AceGen implementation of isothermal models like elastoplasticity (with gradient averaging) as well as thermo-plasticity and non-local thermo-plasticity can be found in [45]. The codes for the isothermal and non-isothermal viscoplasticity are developed basing on the same approach. It is worth mentioning that the time derivative of γ in the viscous term $\xi\dot{\gamma}$ of

the hardening function in Eq. (2.26) is implemented with the backward Euler scheme as follows

$$(3.1) \qquad \dot{\gamma} = \frac{\gamma_n - \gamma_{n-1}}{\Delta t},$$

where γ_n and γ_{n-1} denote the values of the equivalent plastic strain in the current and previous time steps, respectively, and Δt is a time increment in the computational step.

All user subroutines prepared in AceGen by the authors are for three dimensional finite elements, in particular hexahedral elements with linear interpolation of all fields (i.e. mechanical, thermal and the one related to the averaging equation), called H8. The linear interpolation is favourable in terms of computational effort and time, however, it is known that the results for plasticity can be affected by volumetric locking [28]. From among different methods which can be used to prevent the problem we have selected so-called F-bar enhancement [46] which is convenient for AceGen implementation.

4. Simulation of Lueders bands in extended plate

4.1. Test description

The examples considered in this paper are a rectangular plate and a bone-shape sample, both under tension, presented in Fig. 3.

We first focus on the plate benchmark. The three-dimensional FE model is used with one element along the thickness. The dimensions of one-fourth of the plate are $L = 0.1$ m and $W = 0.05$ m. The thickness is 0.0025 m, which due to assumed plain strain constraints is not important. The plane strain state in the three-dimensional model is obtained through kinematic boundary conditions,
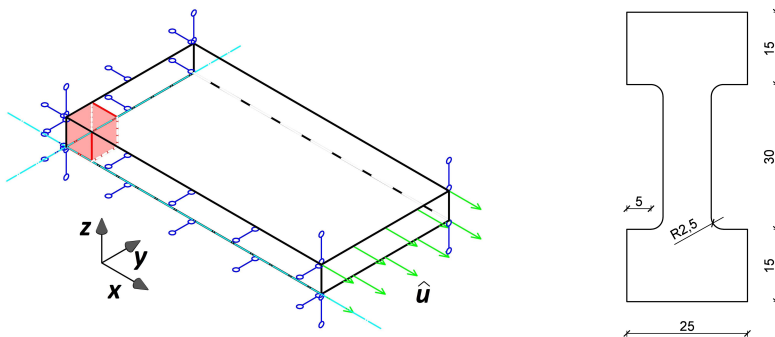
FIG. 3. Analyzed configurations. Left: one-fourth of rectangular plate (imperfection location marked red), boundary conditions block the displacement in thickness direction at every node (dimensions of whole plate $2L \times 2W$ are 20×10 mm). Right: bone-shape sample, dimensions given in mm, thickness is 1 mm.

namely all displacements in the transverse direction are blocked. In this initial test the interest is limited to isothermal conditions.

The plate is stretched in the length direction with the maximum displacement equal to 40 mm ($\Delta L = 0.4L$), multiplied by a loading factor $\lambda \in [0, 1]$. One case for the viscoplastic model was computed for $\Delta L = 0.6L$ (60 mm).

The two models, viscoplastic and gradient-enhanced, are used with the HMH yield function and multil-branch hardening. The computations for the viscoplastic model are carried out for different viscosities and mesh densities. Unless noted otherwise, the simulations are performed for the time period till $t_{max} = 10^{-4}$ s (called maximum tension time), which determines the speed of the loading process. The hardening modulus H_1 is equal to $-0.01\,E$, and the hardening modulus H_2 is equal to $0.005\,E$.

The gradient-enhanced model is employed with different internal lengths and mesh densities. For this model the hardening modulus H_1 is equal to zero, so in the first stage softening is due to damage-like coefficient $1-\omega$, and the hardening modulus H_2 is equal to $0.01\,E$.

Table 1. Material and computation process parameters

Property	Symbol	Value	Unit
Young Modulus	E	$207 \cdot 10^3$	MPa
Poisson ratio	ν	0.29	–
Yield threshold	σ_{y0}	450	MPa
Linear hardening modulus	H_1	$-0.01/0\,E$	MPa
Linear hardening modulus	H_2	$0.005/0.01\,E$	MPa
First threshold	γ_1	0.15	
Second threshold	γ_2	0.3	
Enforced displacement	ΔL	40/60	mm
Viscosity	ξ	$0 \div 0.04$	MPa $\cdot$ s
Maximum tension time	t_{max}	$10^{-4}/10^{-3}/10^{-2}$	s
Ductility	β	10	–
Internal length	l	5/10/20	mm

The test parameters are listed in Table 1, the upper part contains the parameters employed in both models, the middle part includes the parameters for the viscoplastic model and the bottom part for the gradient-enhanced one.

For most tests of the plate sample a mesh with 800 ($40 \times 20 \times 1$) elements H8 is used, called mesh1. A second mesh, called mesh2, contains 3200 ($80 \times 40 \times 1$) cubic elements, and mesh3 contains 12800 ($160 \times 80 \times 1$) elements. To trigger the first shear band an imperfection is introduced, namely the yield strength is reduced to 90% in one corner element of mesh1, see Fig. 3 (left), and in the same volume for denser meshes.

4.2. Numerical results for viscoplastic model

The results of numerical simulations obtained using the viscoplastic description are presented in this section. First, different viscosities are considered.

Four diagrams for the sum of reactions vs the load multiplier are shown in Fig. 4. The diagrams on the left-hand side show the results for different viscosities and for two mesh densities. The top diagram on the right-hand side shows the first part ($\lambda \in [0, 0.2]$) of the left-hand side diagram. The bottom diagram on the right-hand side shows the results for ξ equal to 0.004 MPa·s, mesh1 and two maximum values of imposed displacement ΔL. For zero or small viscosities ($\xi \leq 0.001$) the diagrams exhibit strong softening, then oscillatory response and mesh sensitivity. For $\xi = 0.004$ the softening response weakly depends on mesh density, but the final hardening stage is not visible so the simulation is repeated for larger ΔL, see the figure on the right. For $\xi = 0.01$ and $\xi = 0.04$ the diagrams are mesh-insensitive. However, it is observed that for $\xi = 0.04$ the initial yield strength is strongly exaggerated, which signals excessive regularization.
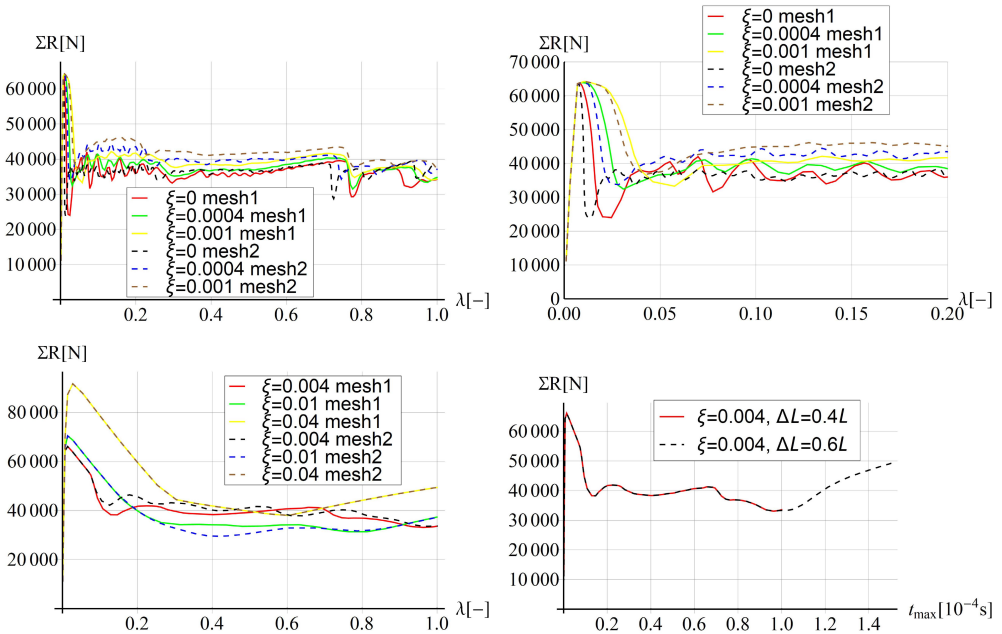
FIG. 4. Sum of reactions vs displacement multiplier for different viscosities, mesh densities and imposed displacement ΔL.

In Figure 5 the distributions of equivalent plastic strain γ and its increment (in computational step) $\Delta\gamma$ as well as plots of $\Delta\gamma$ along the longitudinal specimen axis are presented for ξ equal to 0.004, mesh1 and selected values of the load
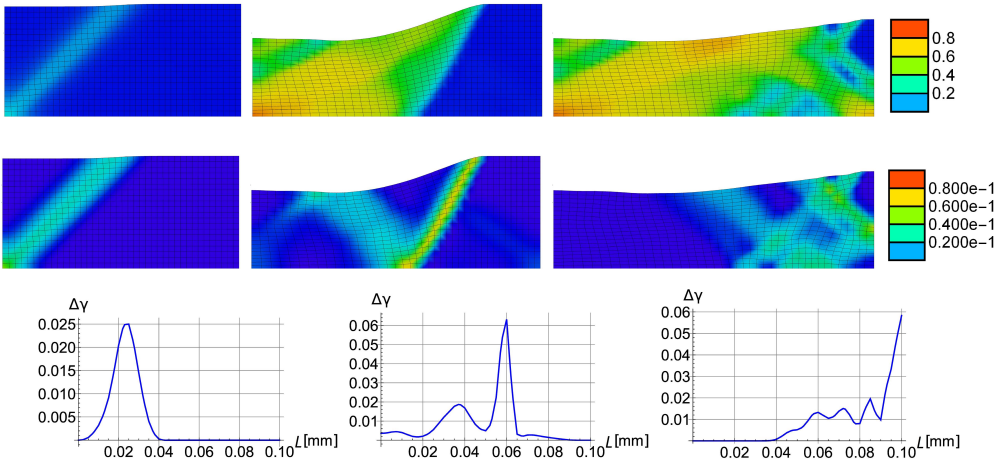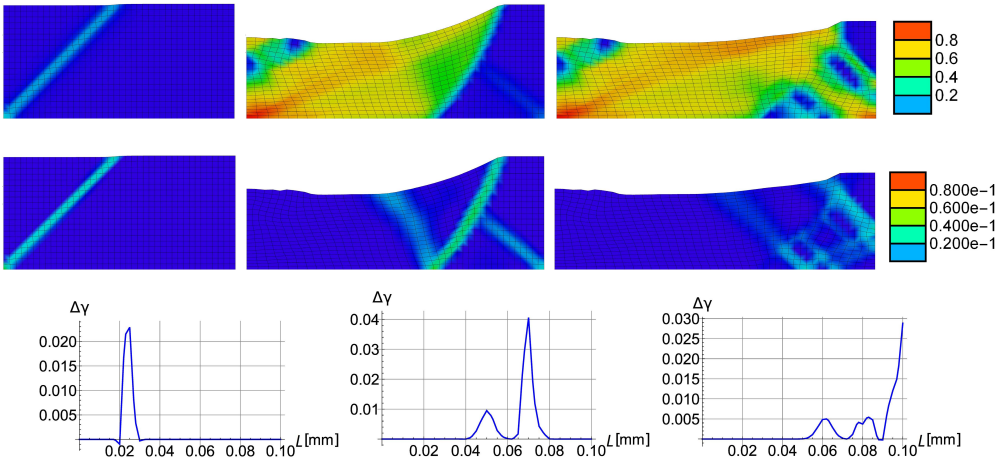
Fig. 5. Results for viscoplastic model with $\xi = 0.004$ for three extension values $\lambda = 0.08$ (left column), $\lambda = 0.66$ (center), and $\lambda = 1$ (right). First row: distributions of γ in deformed plate, second row: distributions of $\Delta\gamma$ in deformed plate, third row: plot of $\Delta\gamma$ along longitudinal axis of undeformed plate.

factor λ. The plots of $\Delta\gamma$ distribution are made for a horizontal cross-section through the centre of the undeformed configuration. Figure 6 is an extension of Fig. 5 for maximum displacement ΔL equal to $0.6L$ and contains only the distributions of $\Delta\gamma$. Figure 7 is prepared in a similar way as Fig. 5 for ten times smaller viscosity $\xi = 0.0004$.

In the first phase of loading a shear band forms (see Fig. 5, left, or Fig. 6, first row, left or Fig. 7, left). Then the shear band starts to move through the sample and it separates into two bands where the process is active, moving in opposite directions (see Fig. 6, first row, right). One of the bands disappears when it reaches the left edge of the sample and then only one band with a perpendicular
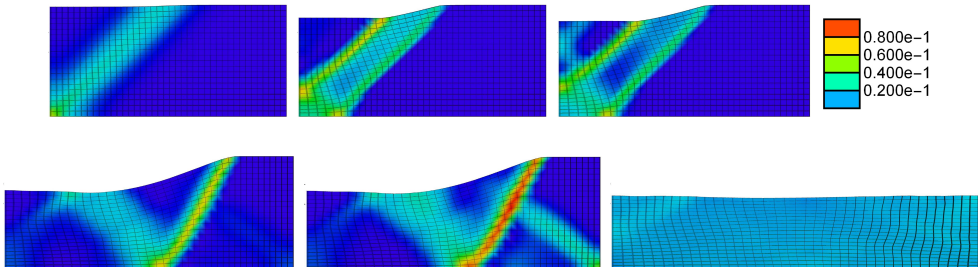
Fig. 6. Distributions of $\Delta\gamma$ for deformed plate, viscoplastic model with $\xi = 0.004$ and $\Delta L = 0.6L$. First row: $\lambda = 0.08$ (left), $\lambda = 0.2$ (center) and $\lambda = 0.24$ (right); second row: $\lambda = 0.66$ (left), $\lambda = 0.68$ (center) and $\lambda = 1.5$ (right).

reflected following band is visible (see Fig. 5 middle or Fig. 6, second row left or Fig. 7 middle). When the band approaches the right edge of the sample, an additional reflected band appears, originated from the right bottom corner (see Fig. 6, second row, middle). When the process finishes, the active zone is visible near the right end of the sample (see Fig. 5, second and third row, right, or Fig. 7, second and third row, right). When the process is longer, the hardening stage is clearly visible (see Fig. 4 right bottom) and at the end almost uniform deformation is obtained (see, Fig. 6, second row, right).

Fig. 7. Results for viscoplastic model with $\xi = 0.0004$ for three extension values $\lambda = 0.02$ (left column), $\lambda = 0.076$ (center) and $\lambda = 1$ (right). First row: distributions of γ for deformed plate; second row: distributions of $\Delta\gamma$ for deformed plate; third row: plot of $\Delta\gamma$ along longitudinal axis of undeformed plate.

Next, the viscoplastic model is considered for different load duration times, i.e. maximum tension times (t_{max}). Two diagrams for the sum of reactions vs the load multiplier are shown in Fig. 8 for viscosity equal to 0.01 (left) and 0.04 (right). As is shown in Fig. 8, a faster process results in a stronger influence of viscosity and stronger regularization. Since viscosity is the only time-dependent effect in the isothermal case, the change of loading duration and hence in the rate of γ is related to the change of the viscosity parameter. In fact, a higher viscosity and smaller t_{max} have a similar influence on the yield strength, cf. Eq. (2.27). It is also mentioned that for small viscosity and/or slower loading (larger t_{max}) some secondary softening stages can be seen in the diagrams. This is due to formation of additional localization bands or patterns during the passage of the main shear band, which has a transient character.

In Fig. 9 the results for the hardening diagram given in Fig. 2 top right, called in brief "soft-hard" $(\gamma_1 = 0.15)$ are compared with the results for the hardening
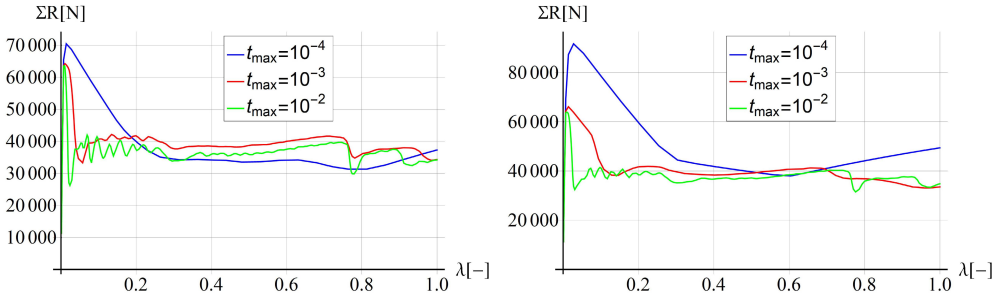
Fig. 8. Sum of reactions vs displacement multiplier for different t_{max} while $\xi = 0.01$ (left) and $\xi = 0.04$ (right).
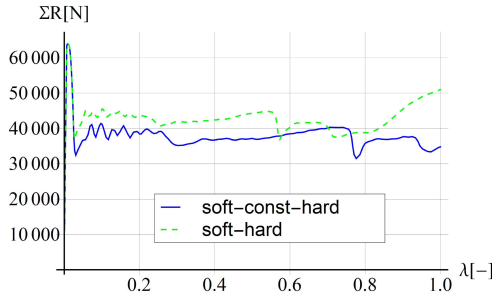

Fig. 9. Sum of reactions vs displacement multiplier for different softening-hardening laws and $\xi = 0.0004$.
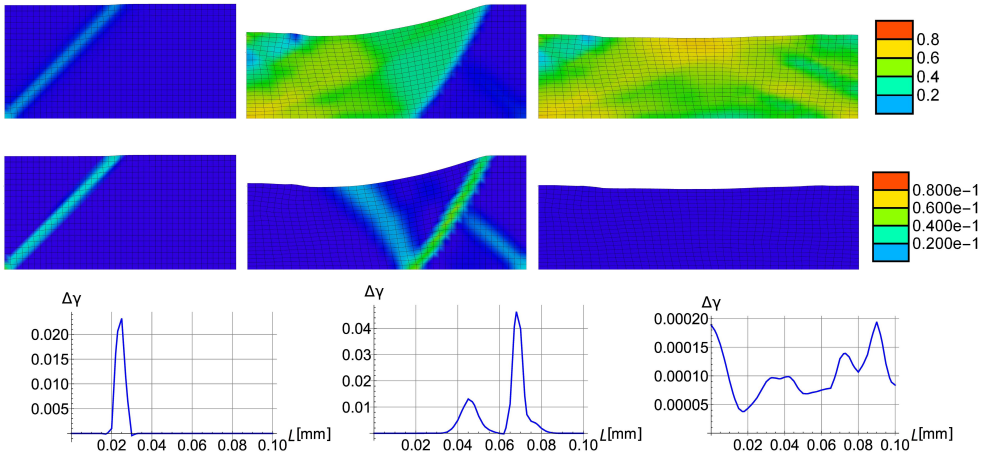

Fig. 10. Results for viscoplastic model with $\xi = 0.0004$ and $\gamma_2 = \gamma_1$, obtained for three extension values $\lambda = 0.02$ (left column), $\lambda = 0.55$ (center) and $\lambda = 1$ (right). First row: distributions of γ for deformed plate; second row: distributions of $\Delta\gamma$ for deformed plate; third row: plot of $\Delta\gamma$ along longitudinal axis for undeformed plate.

function from Fig. 2 top left (called "soft-const-hard") ($\gamma_1 = 0.15$, $\gamma_2 = 0.3$). The diagrams for the two cases are quite similar, however the plateau part for the "soft-hard" case is shifted upwards and a hardening part is observed for $\lambda > 0.8$. This is caused by neglecting the ideal plasticity stage between γ_1 and γ_2, see Fig. 2, and faster hardening. It is however stressed that the almost horizontal branch in the plate response is observed in the absence of the ideal plasticity stage in the hardening diagram.

In Fig. 10 the results for the "soft-hard" diagram matching the results for the "soft-const-hard" diagram in Fig. 7 are presented. It can be seen that now the moving band reaches the opposite end of the sample sooner than for the former case. Moreover, the sample now deforms uniformly at the end of the process when $\lambda = 1$, see the right plot in Fig. 10, contrary to the case presented in the right plot of Fig. 7 where for $\lambda = 1$ a shear band pattern is still visible and hardening does not dominate yet, see the blue line in Fig. 9.

4.3. Numerical results for gradient enhanced model

In this section the analysis is performed using the gradient-enhanced isothermal model. The internal lengths in the performed simulations are 5, 10 and 20 mm (the element size for the coarse mesh1 is 2.5 mm). Usually the internal length l is assumed to be related to a characteristic microstructure dimension. Here it is treated as a numerical regularization parameter, scaling the gradient influence and hence being a measure of nonlocality.
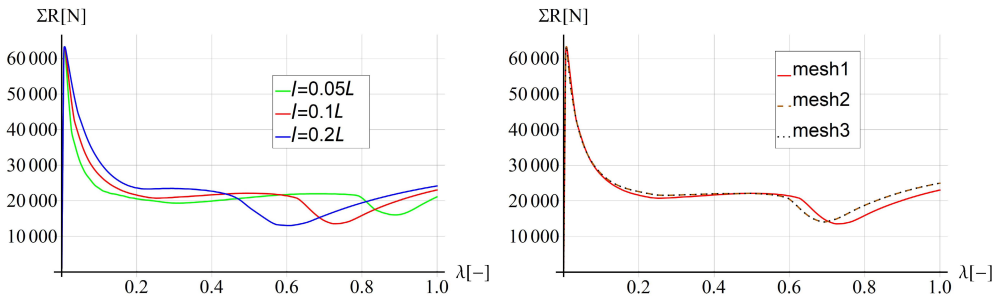

FIG. 11. Sum of reactions vs displacement multiplier for different internal lengths and mesh1 (left) and for different mesh densities for internal length equal to $0.1L$ (right).

Two diagrams for the sum of reactions vs the load multiplier are shown in Fig. 11. The results for different internal lengths are presented on the left-hand side. The diagrams differ as expected up to a cross point about $\lambda = 0.45$ and the response is stiffer for larger length l. A secondary softening appears first for the largest internal length, then for the smaller value. Obviously, the internal

length and related smoothing of the shear band formation influences the simulated evolving localization patterns. On the right-hand side the results for the internal length equal to $0.1L$ and different mesh densities are presented. Discretization sensitivity is hardly visible for the considered three meshes. In general, the response for the gradient-enhanced model is similar to the viscoplastic one. However, the diagrams of the sum of reactions vs load multiplier for the gradient model are smoother than for viscoplasticity, so it seems the gradient enhancement is a stronger regularization than viscosity.

In Fig. 12 the distributions of γ and $\Delta\gamma$ and plots of $\Delta\gamma$ along the longitudinal axis of the configuration are presented for the internal length equal to $0.1L$, mesh1 and different values of λ. Similarly to the viscoplastic computations, in the first phase of loading a shear band forms (see Fig. 12, second row, left). The band starts to travel through the sample and splits into two bands, where the process is active. They move in opposite directions (see Fig. 12, second row, middle and right). The two bands are connected with a perpendicular band, so a pattern of bands reflected on the boundaries is visible. One of the bands vanishes when it reaches the left edge of the sample and only the right band
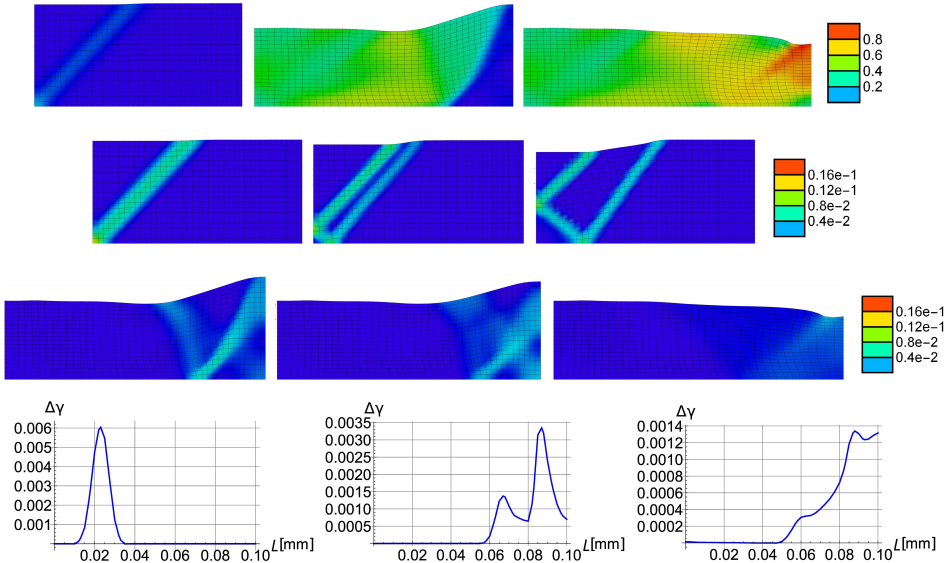

FIG. 12. Results for gradient-enhanced model with internal length $l = 0.1L$. First row: distributions of γ for deformed plate, for three extension values $\lambda = 0.02$ (left), $\lambda = 0.64$ (center) and $\lambda = 1$ (right); second row: distributions of $\Delta\gamma$ for deformed plate, for $\lambda = 0.02$ (left), $\lambda = 0.05$ (center) and $\lambda = 0.14$ (right); third row: distributions of $\Delta\gamma$ for deformed plate, for $\lambda = 0.64$ (left), $\lambda = 0.68$ (center) and $\lambda = 1$ (right); fourth row – plots of $\Delta\gamma$ along horizontal axis for undeformed plate for three extension values $\lambda = 0.02$ (left), $\lambda = 0.64$ (center) and $\lambda = 1$ (right).
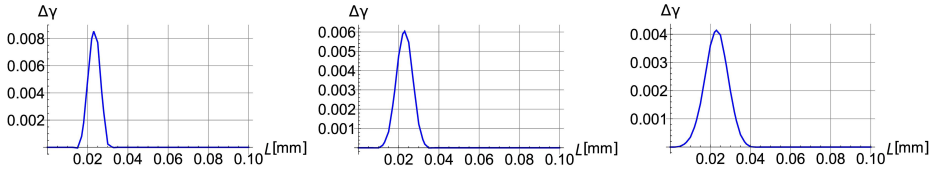
FIG. 13. Plots of $\Delta\gamma$ along horizontal axis for undeformed plate, extension value $\lambda = 0.02$ and different internal lengths from left: $l = 0.05L$, $l = 0.1L$, $l = 0.2L$.

with a reflected following band propagates (see Fig. 12, third row, left). At the end of the process the active zone is diffuse near the right end of the sample and a neck seems to form (see Fig. 12, third row, right). It is stressed that the width of the initially formed shear band, visible in the left diagram showing the cross-section through the $\Delta\gamma$ plot in Fig. 12, depends on the assumed internal length, see Fig. 13.

4.4. Numerical tests for whole plate and viscoplastic model

In this section numerical tests for the whole plate models and selected parameters of the viscoplastic description are presented. Two configurations are used, the configuration C1 for which the boundary conditions are symmetric and identical as for the plate quarter analyzed before (4 imperfect elements in the center are used see Fig. 14 left), but with imposed extension on both sides, and the configuration C2 with imposed displacement on one side, for which the boundary conditions are shown in Fig. 14 right (and only one imperfect element triggers localization). Different imperfection positions are thus assumed, but in each case the total extension of the plate is $0.8L$, where the plate length is $2L$. For configuration C1 the viscosity equal to $\xi = 0.0004$ is used, for the configuration C2 the viscosity is equal to $\xi = 0.004$ and for both configurations the finite element size is identical as for mesh1 presented in the earlier sections.
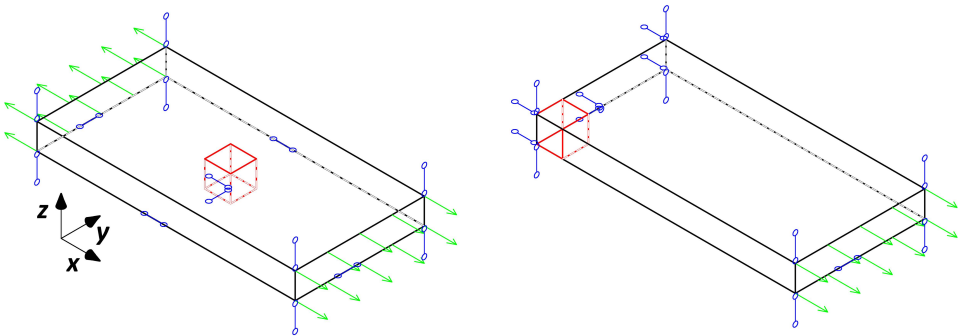

FIG. 14. Boundary conditions for whole plate (imperfection location is marked red). On the left-hand side configuration C1, on the right-hand side configuration C2.

When the plate in the configuration C1 is stretched, a cross-shape band appears first, then it evolves into double bands which move in opposite directions producing an original pattern, see Fig. 15 first row. After the two cross patterns fully separate, reflected bands develop, see Fig. 15 second row left and middle. When the bands approach the ends of the sample, band patterns appear there and the deformation gradually becomes uniform, see Fig. 15 second row right. The plate behaviour in the configuration C1 is similar to the response of one-fourth of the plate.
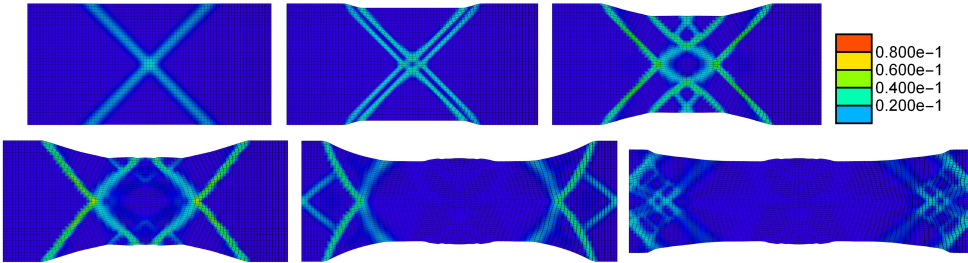
Fig. 15. Distributions of $\Delta\gamma$ for whole deformed plate C1 with imposed symmetry and viscoplastic model with $\xi = 0.0004$. First row: $\lambda = 0.031$ (left), $\lambda = 0.16$ (center) and $\lambda = 0.54$ (right); second row: $\lambda = 0.86$ (left), $\lambda = 1.51$ (center) and $\lambda = 2$ (right).

The model behaviour for the configuration C2 is different due to different boundary conditions and imperfection (symmetry not imposed). First a single band is formed, then it starts to spread and separates into two bands with additional reflected bands, see Fig. 16 first row. Then the formed pattern resembling half of cross-shape with following more distributed localization zone moves to the right, see Fig. 16, second row left and middle. When the pattern reaches the opposite edge of the plate the deformation approaches a uniform state, see Fig. 16 second row right.
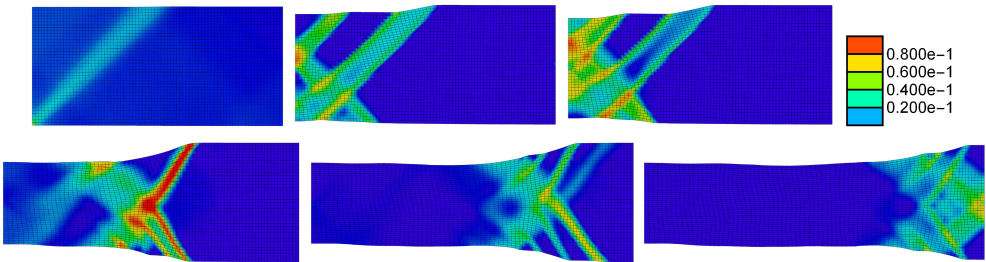

Fig. 16. Distributions of $\Delta\gamma$ for whole deformed plate C2 with corner imperfection and viscoplastic model with $\xi = 0.004$. First row: for $\lambda = 0.14$ (left), $\lambda = 0.34$ (center) and $\lambda = 0.43$ (right); second row: $\lambda = 1.07$ (left), $\lambda = 1.62$ (center) and $\lambda = 2$ (right).

4.5. Numerical tests for extended plate and viscoplastic model with final softening

Finally, one-fourth of the plate is considered with the first multilinear hardening diagram in Fig. 2, enriched with final softening branch to trigger failure. Two new parameters are introduced, $\gamma_3 = 0.45$ and H_3. When γ reaches the third threshold γ_3 the linear hardening modulus becomes negative again ($H_3 = -0.001$ of E). In Fig. 17 the sum of reactions is plotted versus the displacement multiplier. The first band formation, evolution and propagation occur as shown before in Subsecttion 3.2 (see Fig. 18 first row and second row left). When deformation becomes uniform, final softening is triggered and a shear band forms again at the left edge of the plate as a precursor to necking (see Fig. 18 second row, right).
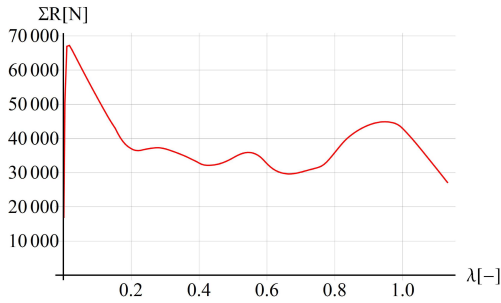

FIG. 17. Sum of reactions vs displacement multiplier for test with final softening branch.
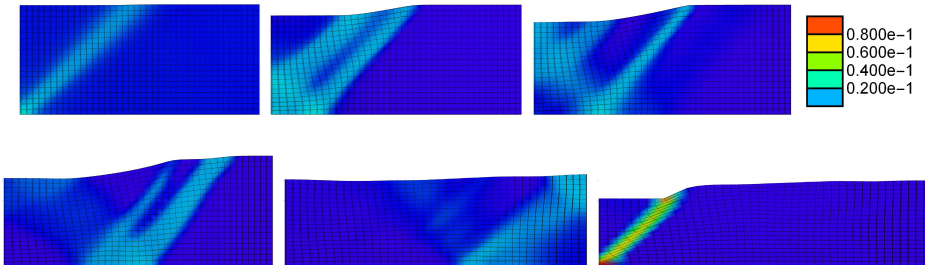

FIG. 18. Distributions of $\Delta\gamma$ for deformed plate quarter, viscoplastic model with $\xi = 0.004$, $\Delta L = 0.6L$ and final softening branch. First row: for $\lambda = 0.12$ (left), $\lambda = 0.24$ (center) and $\lambda = 0.31$ (right); second row: $\lambda = 0.44$ (left), $\lambda = 0.8$ (center) and $\lambda = 1.13$ (right).

5. Simulation of Lueders bands in bone-shape sample

5.1. Test description

The bone-shape sample subjected to tension and its dimensions are presented in Fig. 3 (right). A three-dimensional finite element model is used (no plane strain constrains are applied). The sample is stretched in the length direction with the

maximum displacement equal to 20 mm. The two models, thermo-viscoplasticity and gradient-enhanced thermo-plasticity, are used with the HMH yield function. The boundary conditions for the temperature field are adiabatic (no heat flux through the surface). Thus the temperature evolution in the specimen is due to plastic self heating. The computations for the viscoplastic model are carried out for different viscosities, mesh densities and coefficients of heat conduction. The maximum tension time for the bone-shape sample is 100 s. The hardening modulus H_1 is equal to $-0.005E$, and the hardening modulus H_2 is equal to $0.005E$.

Table 2. Points to compute quadratic hardening parameters.

First value of yield stress	$\sigma_1 = \sigma_{y0}$	450	MPa	First value of γ	γ_1	0
Second value of yield stress	σ_2	375	MPa	Second value of γ	γ_2	0.15
Third value of yield stress	σ_3	450	MPa	Third value of γ	γ_3	0.3

Table 3. Thermal and computation process parameters.

Property	Symbol	Value	Unit
Young Modulus	E	$207 \cdot 10^3$	MPa
Poisson ratio	ν	0.29	-
Yield threshold	σ_{y0}	450	MPa
Linear hardening modulus	H_1	$-0.005/0\ E$	MPa
Linear hardening modulus	H_2	$0.005\ E$	MPa
First threshold	γ_1	0.15	
Quadratic hardening modulus	H_{q1}	$-0.0048\ E$	MPa
Quadratic hardening modulus	H_{q2}	$0.016\ E$	MPa
Enforced displacement	ΔL	20	mm
Maximum tension time	t_{max}	100	s
Conductivity	k	$0 \div 200$	J/(s · K · m)
Heat capacity	c	460	J/(kg · K)
Thermal expansion coeff.	α_T	$12 \cdot 10^{-6}$	1/K
Thermal softening modulus	H_T	0.02	1/K
Dissipation heat factor	χ	0.9	–
Reference temperature	T_0	273.15	K
Viscosity	ξ	$0 \div 400$	MPa · s
Ductility	β	1	–
Internal length	l	0/5/10/20	mm

The gradient-enhanced model is employed with different internal lengths, mesh densities and conductivities. For this model the hardening modulus H_2 is equal to $0.005E$ in isothermal conditions. For the thermo-viscoplastic model

a quadratic hardening function is employed, see Eq. (2.34). The hardening parameters H_{q1} and H_{q2} are calculated from three given points, see Table 2. The material model parameters are listed in Table 3. Since a slower process is now assumed (larger t_{max}), the value of viscosity ξ necessary for regularization is also higher.

For most tests of the bone-shape sample a fine mesh with 8320 hexahedral elements H8 with $\overline{F}$ enhancement [46] is used, called mesh3. For the three-field elements with discretization of displacements $\mathbf{u}$, averaged strain measure z and temperature T linear interpolation is used for all fields. A second mesh, called mesh2, contains 2168 cubic elements, and the coarse mesh1 contains 334 elements. An imperfection is not introduced in the bone-shape sample.

5.2. Numerical results for isothermal viscoplastic model

In Fig. 19 the diagrams for different values of viscosity and for different mesh densities are shown. For two lower values of viscosity a second softening and then hardening stage can be seen between λ equal to 0.3 and 0.4. This is caused by different types of localization when two bands are formed at the beginning of the process and in that interval they merge, see Fig. 21.

In Figs. 20 and 21 the distributions of $\dot{\gamma}$ ($\Delta\gamma/\Delta t$) in the bone-shape sample are presented. The first two plots from the left in Fig. 20 show localization of a single cross-shape band pattern in the middle of the sample. When the softening stage is finished two band patterns occur and move in opposite directions (next four plots). At the end of the next phase, when hardening dominates, the deformation in the extending process zone becomes uniform (last plot).

The first plot from the left in Fig. 21 shows localization of a double cross-shape band pattern in the central part of the sample. When the softening stage ends four band patterns form and move in opposite directions (next three plots). When the bands merge a single cross-shape can be seen in the middle of the
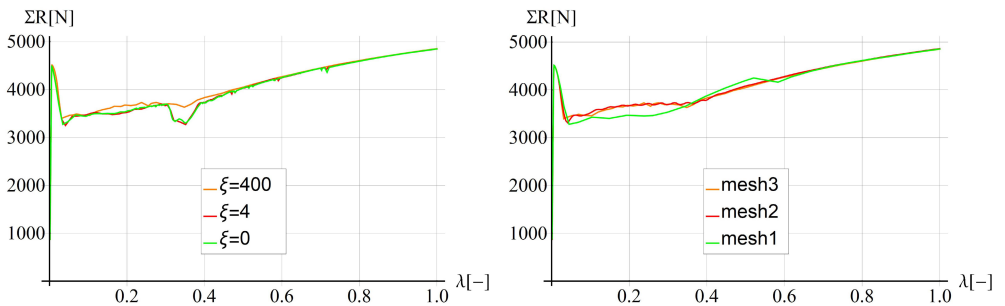

Fig. 19. Sum of reactions vs displacement multiplier for different viscosities and mesh3 (left) and for different mesh densities while viscosity is equal to 400.0 (right).
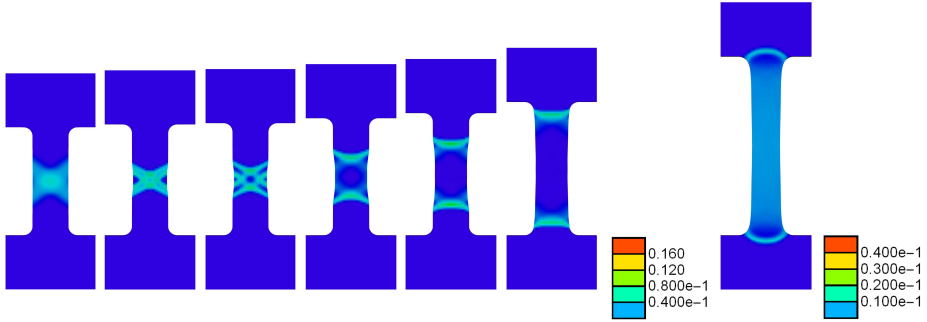
Fig. 20. Distributions of $\dot{\gamma}$ for viscosity equal to 400 and mesh3, patterns for λ equal to (from left) 0.01, 0.05, 0.07, 0.14, 0.21, 0.37, 1.
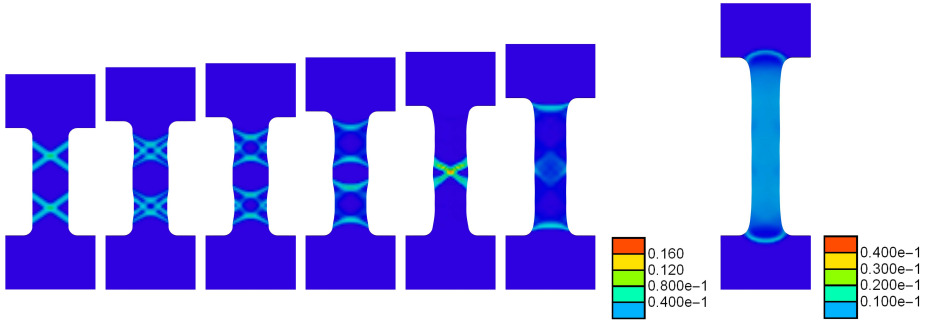

Fig. 21. Distributions of $\dot{\gamma}$ for viscosity equal to 4.0 and mesh3, patterns for λ equal to (from left) 0.01, 0.11, 0.16, 0.24, 0.32, 0.43, 1.

sample, which dominates the process (fifth plot, see also Fig. 19, left plot). When the two bands merge, the second softening stage is over and the process continues (sixth plot). At the end of the next phase deformation becomes uniform due to hardening (last plot).

5.3. Numerical results for gradient-enhanced model

In Fig. 22 the diagrams for different values of internal length and for different mesh densities are shown. The internal length dependence is small and mesh sensitivity for the gradient model is hardly visible. In Fig. 23 the distributions of $\dot{\gamma}$ ($\Delta\gamma/\Delta t$) are presented. The first three plots from the left show localization of a single cross-shape band pattern in the middle of the sample. When the softening stage ends two band patterns (plastic fronts) appear and propagate in opposite directions. At the end of the hardening phase, deformation becomes uniform similarly to the previous simulations.
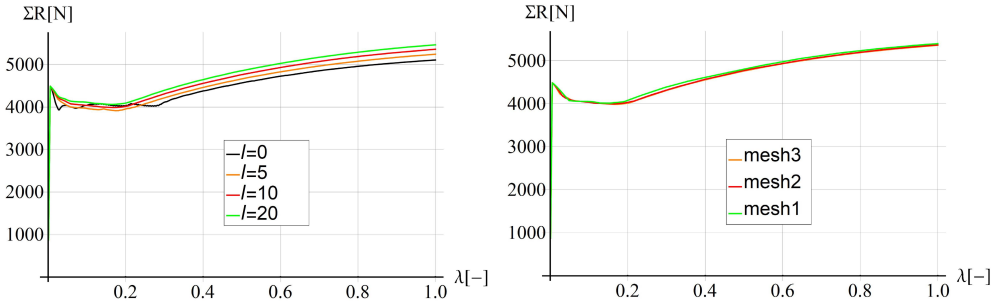
Fig. 22. Sum of reactions vs displacement multiplier for different internal lengths and mesh3 (left) and for different mesh densities for internal length equal to 10 mm (right).
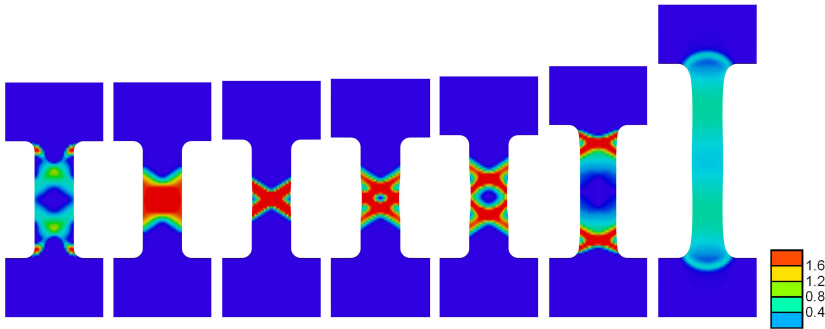

Fig. 23. Distributions of $\dot{\gamma}$ for internal length equal to 10 mm and mesh3, patterns for λ equal to (from left) 0.005, 0.006, 0.02, 0.05, 0.08, 0.2, 0.73, 1.

5.4. Numerical results for thermo-viscoplastic model

In Fig. 24 the diagrams for different values of viscosity and conductivity and for different mesh densities are shown. If not stated differently conductivity k equal to 50 J/(s·K·m) is assumed. The diagrams for three values of viscosity are very similar, but oscillations are smaller for larger values of ξ. Some oscillations are also visible for conductivity k equal to 0. The heat conduction provides an additional regularization (the first one is viscosity), therefore for k larger than 50 the differences between diagrams are minor. The slopes of lines are slightly different for different values of k and differences are noticeable on horizontal parts of diagrams. The differences gradually vanish during the hardening stage. The oscillations can partly be caused by thermal softening and for the lower value of k the conductivity is not high enough to prevent them.

In Fig. 25 the evolution of $\dot{\gamma}$ distribution in the bone-shape sample is presented. The behaviour is similar to what can be observed for the isothermal model (see Fig. 20 left). First a cross-shape band pattern occurs in the middle
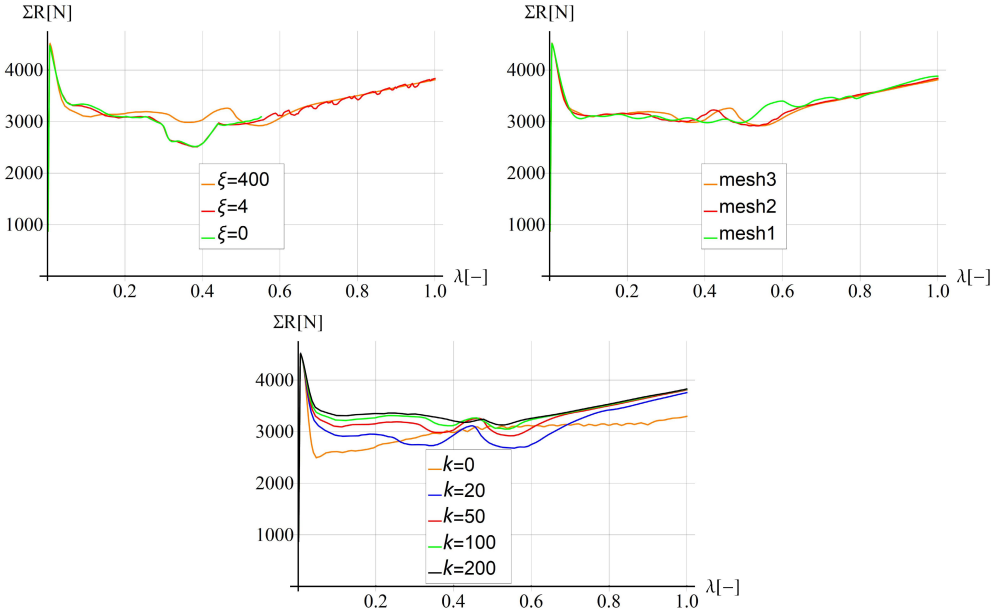
Fig. 24. Sum of reactions vs displacement multiplier for different viscosities (top, left) while $k = 50$, different mesh densities for $k = 50$ and $\xi = 400$ (top, right) and different conductivities for $\xi = 400$ (bottom, right).

of the sample. Then two band patterns form and move in opposite directions. Due to the oscillations this process is not symmetric. One of the bands almost disappears (see Fig. 25, fourth pattern from left) and they move with different speeds (see Fig. 25 fifth from left). In Fig. 26 the distributions of relative temperature $T - T_0$ in the bone-shape sample are presented. For k equal to 0 (adiabatic case) the temperature field is localized, contrary to the case when the value of conductivity is higher and the temperature field is diffuse.
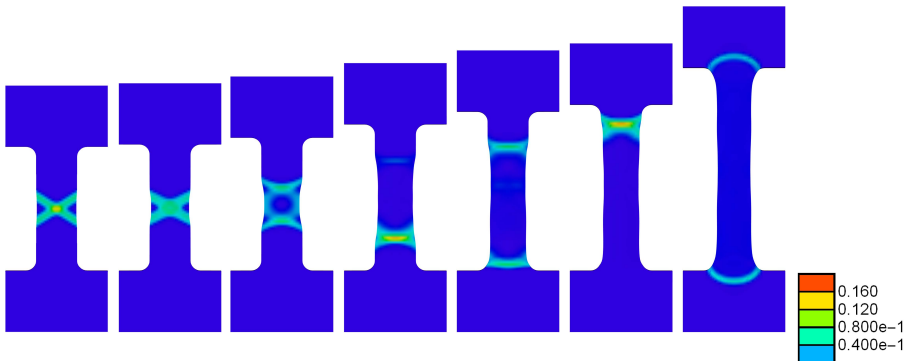

Fig. 25. Distributions of $\dot{\gamma}$ for $\xi = 400$, $k = 50$ and mesh3, plots for λ equal to (from left) 0.03, 0.06, 0.14, 0.3, 0.46, 0.54, 1.
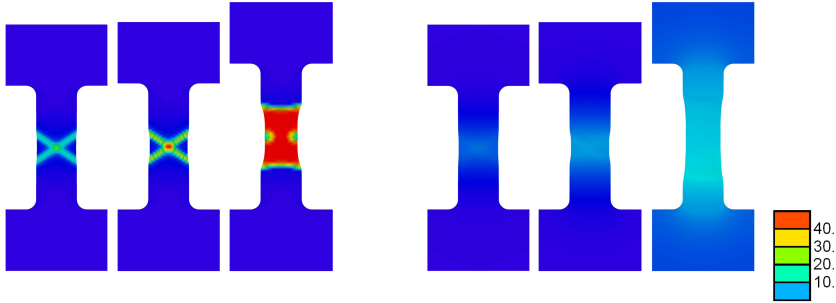
FIG. 26. Distributions of $T - T_0$ for $\xi = 400$, mesh3 and $k = 0$ (left, three plots) and $k = 100$ (right, three plots), plots for λ equal to (from left) 0.03, 0.06, 0.3 (the same steps are used for both cases).

5.5. Numerical results for gradient-enhanced thermo-plastic model

Finally, the Lueders bands propagation in the bone-shape sample is simulated using the gradient-enhanced thermo-plastic model. In Fig. 27 diagrams for different values of internal length and conductivity, and for different mesh densities are shown. The oscillations are stronger than observed in Fig. 24 for the
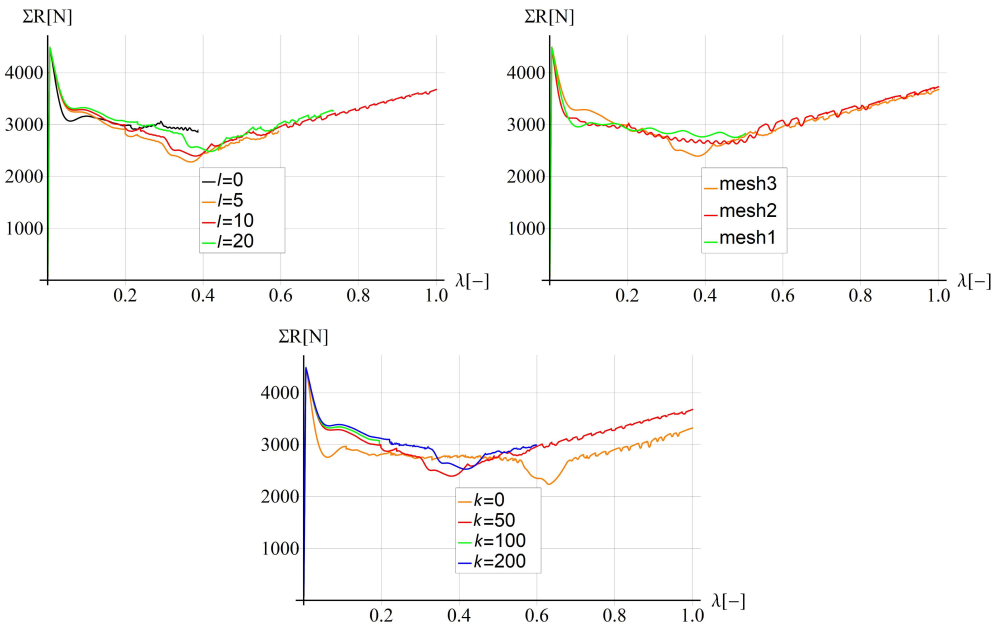

FIG. 27. Sum of reactions vs displacement multiplier for different internal length for mesh3, $k = 50$ (top, left), for different mesh densities for $l = 10$, $k = 50$ (top, right), and for different conductivities for mesh3, $l = 10$ (bottom).

thermo-viscoplastic model. Time steps used for calculations are much smaller due to problems with convergence. We can then observe small sensitivity to the mesh size and the internal length (only for $l = 0$ the response is originally more brittle and the simulation diverges for $\lambda = 0.39$).
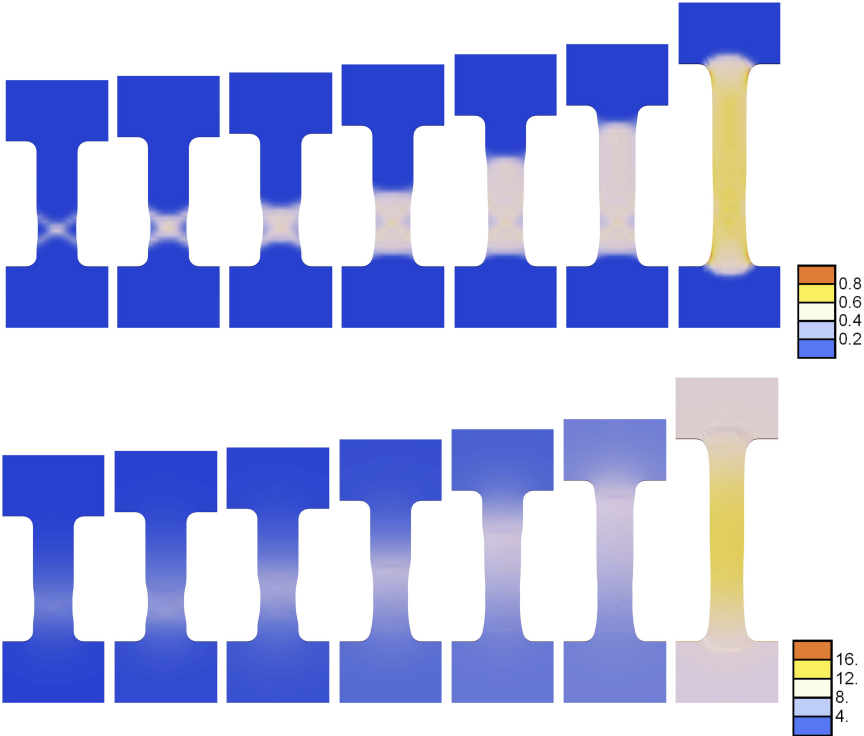

Fig. 28. First row: distributions of γ. Second row: distributions of $T - T_0$. Assumed $l = 10$, $k = 50$, mesh2 and λ equal to (from left) 0.05, 0.1, 0.14, 0.24, 0.36, 0.49, 1.

In Fig. 28 the distributions of plastic strain measure γ and temperature $T - T_0$ are shown. The localisation starts at the bottom of the sample probably due to a numerical imperfection. Then plastic fronts form and start to move. At the end of the process a uniform deformation is visible in the middle part of the sample.

For $k = 0$ (see Fig. 27 bottom) a much lower diagram is simulated which suggests the regularization with $l = 10$ is insufficient in the adiabatic case $k = 0$.

6. Conclusions

The goal of this paper has been to simulate the propagative instability phenomenon called Lueders bands using two regularized large strain models: viscoplasticity and gradient-enhanced plasticity. The Huber–Mises–Hencky yield

function with multi-branch hardening has been employed. Moreover, the influence of temperature increase (and the related phenomena: conduction of thermal energy, plastic heating and thermal softening) has additionally been examined. AceGen and AceFEM numerical packages for Wolfram Mathematica have been used to implement the models. Computations have been performed for an extended rectangular plate in an isothermal regime and for a bone-shape sample in isothermal and conductive conditions. A parametric study has been performed concerning the value of viscosity and the internal length for the two respective models, and also the heat conductivity. Three mesh densities have been used to verify discretization sensitivity.

It has been observed that the elastic-plastic model with multi-branch hardening enables the simulation of Lueders bands. It has been shown that the band pattern evolves in the plate or the bone-shape sample starting from an initially formed shear bands related to the softening stage in the material response. As expected, the width of the shear bands grows with increasing viscosity and internal length, respectively.

In the rectangular plate the plastic zone broadens when softening finishes, reflections of the bands on specimen boundaries are observed and the dominating shear band propagates along the specimen. The influence of viscosity on the band formation and evolution is significant. A large viscosity results in an excessive load-carrying capacity of the specimen at the beginning of the process. When regularization provided by viscosity is not sufficient, different band patterns, for instance a double-band pattern, can be seen in the sample. When the process duration is larger (and hence the process rate is smaller), a stronger viscosity is needed to regularize the response. It has been confirmed that for a large enough viscosity a spurious mesh dependence of the results is removed. However, it has also been shown that the regularization reduces oscillations present in load-displacement diagrams.

Further, the consequences of modelling of a quarter of the plate due to symmetry have been addressed and the simulations have been repeated for a full-size configuration, thereby examining the influence of boundary conditions. Next to Lueders-type response to a softening-constant-hardening yield strength function, a softening-hardening function and an additional final softening stage leading to failure have also been simulated. It is confirmed that the horizontal branch in the hardening input is not necessary in the model to represent the plateau in the Lueders-type response, which has a structural character and is caused by an interaction of softening and hardening at the point level and propagating localization.

Concerning the gradient-enhanced model, in the considered range of internal length scales the influence of gradients on the results is visible but not as strong as the influence of viscosity. Mesh sensitivity for the gradient model is not visible in

the first softening phase, the diagrams for the plate start to differ when secondary softening appears due to a change of instability mode.

The results for bone-shape sample in the isothermal case are quite similar, although depending on the viscosity one now observes the propagation of different cross-shape shear band patterns. The results of this test performed with the gradient model show small influence of the internal length. For both models mesh sensitivity is hardly visible.

In the thermo-mechanical model thermal softening of the yield strength with temperature increase is included, which is an additional instability source, resulting in stronger response oscillations. Some mesh sensitivity is also visible even for significant viscosity and larger internal lengths. In this paper the heat conduction is not treated as a localization limiter, although its regularizing effect is recorded, i.e. larger conductivity results in more ductile load-extension diagrams and diffuse distribution of temperature changes caused by plastic heating. It is found that for the assumed set of data the influence of the plastic heating and conduction on the Lueders bands propagation is not significant.

The research has several open ends. Most importantly, a series of laboratory experiments is planned to validate the model parameters and get a deeper insight into the rate-sensitivity of the phenomenon. Although the Lueders bands are observed at room temperature, a broader analysis of the influence of the thermal phenomena on the process should be made using the fully coupled thermo-mechanical description. Moreover, dynamic loading conditions could be considered in simulations of propagative instabilities [47]. Simulations of the PLC effect which in certain conditions follows the transient Lueders effect can then be performed.

References

1. A.H. Cottrell, *The Mechanical Properties of Matter*, John Wiley & Sons, New York, 1964.

2. Y. Estrin, L.P. Kubin, *Spatial coupling and propagative plastic instabilities*, [in:] H.-B. Mühlhaus [ed.], *Continuum Models for Materials with Microstructure*, John Wiley & Sons, Chichester, 1995, 395–450.

3. J.F. HALLAI, S. KYRIAKIDES, *Underlying material response for Lüders-like instabilities*, International Journal of Plasticity, **47**, 1–12, 2013.

4. A. NEEDLEMAN, *Material rate dependence and mesh sensitivity in localization problems*, Computer Methods in Appllied Mechanics and Engineering, **67**, 69–86, 1988.

5. W.M. WANG, L.J. SLUYS, R. DE BORST, *Viscoplasticity for instabilities due to strain softening and strain-rate softening*, International Journal for Numerical Methods in Engineering, **40**, 20, 3839–3864, 1997.

6. T. ŁODYGOWSKI, *Theoretical and numerical aspects of plastic strain localization*, Technical Report Monography, **312**, Poznań University of Technology, Poznań, 1996.

7. R.H.J. PEERLINGS, R. DE BORST, W.A.M. BREKELMANS, J.H.P. DE VREE, *Gradient-enhanced damage for quasi-brittle materials*, International Journal for Numerical Methods in Engineering, **39**, 3391–3403, 1996.

8. M.G.D. GEERS, *Finite strain logarithmic hyperelasto-plasticity with softening: a strongly non-local implicit gradient framework*, Computer Methods in Applied Mechanics and Engineering, **193**, 3377–3401, 2004.

9. J. LEMONDS, A. NEEDLEMAN, *Finite element analyses of shear localization in rate and temperature dependent solids*, Mechanics of Materials, **5**, 339–361, 1986.

10. A. NEEDLEMAN, *Continuum mechanics studies of plastic instabilities*, Revue de Physique Appliquee, **23**, 585–593, 1988.

11. B. DODD, Y. BAI, *Introduction to Adiabatic Shear Localization*, Imperial College Press, London, revised edition, 2015.

12. M.K. DUSZEK, P. PERZYNA, E. STEIN, *Adiabatic shear band localization in elastic-plastic damaged solids*, International Journal of Plasticity, **8**, 4, 361–384, 1992.

13. A. MOLINARI, *Adiabatic shear banding as an example of viscoplastic flow instability*, [in:] G.A. Maugin, R. Drouot, and F. Sidoroff [eds.], *Continuum Thermomechanics Solid Mechanics and Its Applications*, **76**, 313–330, Springer, Dordrecht, 2000.

14. H. LOUCHE, A. CHRYSOCHOOS, *Thermal and dissipative effects accompanying Lüders band propagation*, Materials Science and Engineering, A, **307**, 12, 15–22, 2001.

15. J. ZHANG, Y. JIANG, *Lüders bands propagation of 1045 steel under multiaxial stress state*, International Journal of Plasticity, **21**, 3, 651–670, 2005.

16. V.I. DANILOV, V.V. GORBATENKO, L.B. ZUEV, *On the kinetics of mobile Chernov–Lüders band fronts*, AIP Conference Proceedings, **1783**, 1, 020034, 2016.

17. H.B. SUN, F. YOSHIDA, X. MA, T. KAMEI, M. OHMORI, *Finite element simulation on the propagation of Lüders band and effect of stress concentration*, Materials Letters, **57**, 21, 3206–3210, 2003.

18. S. KYRIAKIDES, A. OK, E. CORONA, *Localization and propagation of curvature under pure bending in steel tubes with Lüders bands*, International Journal of Solids and Structures, **45**, 10, 3074–3087, 2008.

19. M. MAZIÈRE, C. LUIS, A. MARAIS, S. FOREST, M. GASPÈRINI, *Experimental and numerical analysis of the Lüders phenomenon in simple shear*, International Journal of Solids and Structures, **106**–**107**, 305–314, 2017.

20. M. Rezaee-Hajidehi, S. Stupkiewicz, *Gradient-enhanced model and its micromorphic regularization for simulation of Lüders-like bands in shape memory alloys*, International Journal of Solids and Structures, **135**, 208–218, 2018.

21. W.M. Wang, *Stationary and propagative instabilities in metals – a computational point of view*, Ph.D. dissertation, Delft University of Technology, Delft, 1997.

22. L.J. Sluys, W.-M. Wang, *Macroscopic modelling of stationary and propagative instabilities*, [in:] de Borst and van der Giessen, *Material Instabilities in Solids*, John Wiley & Sons, Chichester, pp. 489–505, 1998.

23. R. de Borst, *Some recent issues in computational failure mechanics*, International Journal for Numerical Methods in Engineering, **52**, 63–95, 2001.

24. D. Bigoni, *Nonlinear Solid Mechanics: Bifurcation Theory and Material Instability*, Cambridge University Press, Cambridge, 2012.

25. M. Mazière, S. Forest, *Strain gradient plasticity modeling and finite element simulation of Lüders band formation and propagation*, Continuum Mechanics and Thermodynamics, **27**, 1–2, 83–104, 2015.

26. B. Wcisło, J. Pamin, *Local and non-local thermomechanical modeling of elastic-plastic materials undergoing large strains*, International Journal of Numerical Methods in Engineering, **65**, 102–124, 2017.

27. B. Wcisło, J. Pamin, K. Kowalczyk-Gajewska, *Gradient-enhanced damage model for large deformations of elastic-plastic materials*, Archives of Mechanics, **65**, 5, 407–428, 2013.

28. J. Pamin, B. Wcisło, K. Kowalczyk-Gajewska, *Gradient-enhanced large strain thermoplasticity with automatic linearization and localization simulations*, Journal of Mechanics of Materials and Structures, **12**, 1, 123–146, 2017.

29. J. Korelc, *Automation of primal and sensitivity analysis of transient coupled problems*, Computational Mechanics, **44**, 631–649, 2009.

30. J. Korelc, *Automation of the finite element method*, [in:] P. Wriggers [ed.], Nonlinear Finite Element Methods, 483–508, Springer-Verlag, Berlin Heidelberg, 2008.

31. J. C. Simo, *A framework for finite strain elastoplasticity based on maximum plastic dissipation and the multiplicative decomposition: Part 1. Continuum formulation*, Computer Methods in Applied Mechanics and Engineering, **66**, 199–219, 1988.

32. P.A. Wriggers, C. Miehe, M. Kleiber, J.C. Simo, *On the coupled thermomechanical treatment of necking problems via finite element methods*, International Journal of Numerical Methods in Engineering, **33**, 869–883, 1992.

33. E.H. Lee, *Elastic plastic deformation at finite strain*, ASME Transactions Journal of Applied Mechanics, **36**, 1–6, 1969.

34. E.H. Lee, D.T. Liu, *Finite-strain elastic-plastic theory with application to plane-wave analysis*, Journal of Applied Physics, **38**, 19–27, 1967.

35. S.C.H. Lu, K.S. Pister, *Decomposition of deformation and representation of the free energy function for isotropic thermoelastic solids*, International Journal of Solids and Structures, **11**, 927–934, 1975.

36. M. Ristinmaa, M. Wallin, N.S. Ottosen, *Thermodynamic format and heat generation of isotropic hardening plasticity*, Acta Mechanica, **194**, 103–121, 2007.

37. J.C. Simo, C. Miehe, *Associative coupled thermoplasticity at finite strains: Formulation, numerical analysis and implementation*, Computer Methods in Applied Mechanics and Engineering, **98**, 1, 41–104, 1992.

38. F. Oka, H.-B. Mühlhaus, A. Yashima, K. Sawada, *Quasi-static and dynamic characteristics of strain gradient dependent non-local constitutive models*, [in:] de Borst and van der Giessen, Isntabilities in Solids, John Wiley & Sons, Chichester, 387–404, 1998.

39. S. Okazawa, *Structural bifurcation for ductile necking localization*, International Journal of Nonlinear Mechanics, **45**, 35–41, 2009.

40. J.C. Simo, *Numerical analysis and simulation of plasticity*, [in:] P.G. Ciarlet and J.L. Lions [eds.], *Handbook of Numerical Analysis. Numerical methods for solids (Part 3)*, vol. VI, pages 183–499, Elsevier Science, Boca Raton, 1998.

41. C. Miehe, *Entropic thermoelasticity at finite strains. Aspects of the formulation and numerical implementation*, Computer Methods in Applied Mechanics and Engineering, **120**, 243–269, 1995.

42. G.I. Taylor, H. Quinney, *The latent energy remaining in a metal after cold working*, Proceedings of the Royal Society of London, Series A, **143**, 307–326, 1934.

43. B. Wcisło, *Simulations of thermal softening in large strain thermoplasticity with degradation*, Engineering Transactions, **4**, 64, 563–572, 2016.

44. Z.P. Bažant, M. Jirásek, *Nonlocal integral formulations and damage: Survey of progress*, ASCE Journal of Engineering Mechanics, **128**, 11, 1119–1149, 2002.

45. B. Wcisło, *Large Strain Thermomechanical Material Models Accounting for Inelasticity, Instabilities and Gradient Enhancement*, Ph.D. dissertation, Cracow University of Technology, Cracow, 2017.

46. E.A. de Souza Neto, D. Peric, D.R.J. Owen, *Computational Methods for Plasticity. Theory and Applications*, John Wiley & Sons, Chichester, UK, 2008.

47. L.J. Sluys, *Wave Propagation, Localization and Dispersion in Softening Solids*, Ph.D. dissertation, Delft University of Technology, Delft, 1992.

48. R. de Borst, E. van der Giessen [eds.], *Material Instabilities in Solids*, IUTAM, John Wiley & Sons, Chichester, 1998.